Targeting of Primary Breast Cancers and Metastases in a Transgenic Mouse Model Using Rationally Designed Multifunctional SPIONs

Forrest M. Kievit,[†] Zachary R. Stephen,[†] Omid Veiseh,[†] Hamed Arami,[†] Tingzhong Wang,[‡] Vy P. Lai,[§] James O. Park,[⊥] Richard G. Ellenbogen,[∥] Mary L. Disis,[§] and Miqin Zhang[†,∥,*]

[†]Department of Materials Science & Engineering, University of Washington, Seattle, Washington 98195, United States, [‡]Department of Neurosurgery, The Fourth Affiliated Hospital of China Medical University, Shenyang, Liaoning 110032, China, [§]Division of Oncology, University of Washington, Seattle, Washington 98195, United States, [⊥]Department of Surgery, University of Washington, Seattle, Washington 98195, United States, and [∥]Department of Neurological Surgery, University of Washington, Seattle, Washington 98195, United States

ABSTRACT Breast cancer remains one of the most prevalent and lethal malignancies in women. The inability to diagnose small volume metastases early has limited effective treatment of stage 4 breast cancer. Here we report the rational development and use of a multifunctional superparamagnetic iron oxide nanoparticle (SPION) for targeting metastatic breast cancer in a transgenic mouse model and imaging with magnetic resonance (MR). SPIONs coated with a copolymer of chitosan and polyethylene glycol (PEG) were labeled with a fluorescent dye for optical detection and conjugated with a monoclonal antibody against the neu receptor (NP-neu). SPIONs labeled with mouse IgG were used as a nontargeting control (NP-IgG). These SPIONs had desirable physiochemical properties for *in vivo* applications such as near neutral zeta potential and hydrodynamic size around 40 nm and were highly stable in serum containing medium. Only NP-neu showed high uptake in neu expressing mouse mammary carcinoma (MMC) cells which was reversed by competing free neu antibody, indicating their specificity to the neu antigen. *In vivo*, NP-neu was able to tag primary breast tumors and significantly, only NP-neu bound to spontaneous liver, lung, and bone marrow metastases in a transgenic mouse model of metastatic breast cancer, highlighting the necessity of targeting for delivery to metastatic disease. The SPIONs provided significant contrast enhancement in MR images of primary breast tumors; thus, they have the potential for MRI detection of micrometastases and provide an excellent platform for further development of an efficient metastatic breast cancer therapy.

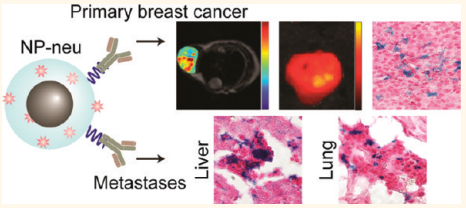

KEYWORDS: iron oxide · nanoparticle · genetically engineered mouse model · HER2/neu · theranostics · breast cancer · metastases

With 207090 new cases and 39840 resultant deaths estimated in 2010, breast cancer is the second most common malignancy and the second leading cause of cancer-related deaths among women in the U.S.[1] Despite better understanding of the molecular basis of cancer and advances in treatments, the number of breast cancer deaths per year has shown only a modest decrease over the past 20 years (43391 breast cancer deaths in 1990 to 39840 in 2010).[2] The greatest challenge has been the early detection and treatment of metastases, as metastatic disease accounts for most of the cancer mortality.[3−5] Current treatment consists of surgical resection and radiotherapy for local treatment of the primary cancer and nodal disease and liberal administration of chemotherapy for locoregional and distant metastatic disease. Unfortunately, more than 80% of breast cancer patients are treated with toxic chemotherapies, whereas only 40% of them have metastatic disease.[3] This overtreatment decreases quality of life of patients and imposes added strain to the health care system; however, it is still employed given the inability to effectively detect early stage metastatic disease.

Nanotechnology provides a unique opportunity to generate more effective and less invasive diagnostic and treatment strategies through synthesis of multifunctional nanoparticles (NPs) that provide molecularly targeted therapy.[6] Furthermore, the nanoscale imparts unique physical properties on materials used for synthesis such as optical properties on noble metal NPs, fluorescence properties on semiconductor NPs, and superparamagnetic properties on metal oxide NPs that can be exploited for imaging purposes. Of the nanomaterials studied, superparamagnetic iron oxide nanoparticles (SPIONs) have garnered significant attention owing to their biodegradability and inherent contrast enhancement in magnetic resonance imaging (MRI).[7,8] Ideally, a SPION

* Address correspondence to mzhang@u.washington.edu.

Received for review December 25, 2011 and accepted February 10, 2012.

Published online February 10, 2012
10.1021/nn205070h

used for breast cancer detection should have: (1) sufficient functional groups on the surface of the SPION for attachment of targeting agents; (2) hydrodynamic size between 10 and 100 nm to prevent elimination from the blood through the kidneys and liver; (3) near-neutral zeta-potential to minimize nonspecific interaction with blood components and off-target cells; and (4) high stability in physiologically relevant media. Furthermore, the targeting ligand attached to the surface of the SPION must have a high affinity to breast cancer cell receptors to maximize uptake in target cells while minimizing nonspecific uptake in off-target cells.

Neu (HER2/neu in humans or ErbB2) is a proto-oncogene that is overexpressed in up to 30% of breast cancers. Patients harboring HER2/neu positive breast cancers generally have a poorer prognosis because of the high aggressiveness and chemoresistance of the disease.[9,10] Neu targeting is a promising strategy for detecting aggressive metastatic breast cancer,[11] and trastuzumab, a HER2/neu antibody, is currently used for clinical treatment.[12] A number of different SPION formulations have been developed to target neu over-expressing breast cancers for imaging and therapies,[13−16] indicating that neu is a good tumor-specific ligand for breast cancer cells. However, clinical translation of SPIONs for breast cancer detection has been slow due to the challenges in meeting all the requirements of SPIONs as contrast agents, including unfavorable pharmacokinetic properties with accumulation of significant amounts of particles in nontarget tissues and insignificant amounts in tumor tissues, and more importantly to insufficient preclinical testing using artificial xenograft models. Transgenic mouse models more faithfully mimic human disease than xenograft models and offer an improved preclinical model for SPION testing.[17] Tumors develop in the tissue of interest and recapitulate the evolution of the microenvironment observed in the human disease. Furthermore, unlike the nude and SCID mice used for xenografts, transgenic mice have an intact immune system. Importantly, the development and metastatic progression of the disease mimic what would be seen in a clinical setting. Preclinical testing in transgenic mice is expected to accelerate translation since only more robust SPIONs will make it to clinical testing and be less likely to fail in these later, more costly stages.[17]

Here we report the development of a SPION-based formulation with the physiochemical properties required for targeting breast cancers overexpressing neu receptors, and with the required properties for *in vivo* imaging as demonstrated in a neu transgenic mouse model. The nanoparticle formulation is made of a SPION core coated with a copolymer of chitosan-grafted PEG (namely NPCP) and conjugated with neu antibody. Chitosan is a biodegradable natural polymer consisting of multiple functional groups that provide anchoring for drugs, imaging agents, and targeting moieties. PEG is a commonly used polymer that provides steric stabilization for increased colloidal stability and decreased immune recognition. We test the ability of this SPION to specifically recognize breast cancer cells and tag breast tumors in transgenic mice for detection in MRI. Furthermore, we investigate the extent of micrometastases labeling in the lungs, livers, and bone marrow from these transgenic mice.

RESULTS AND DISCUSSION

NP Synthesis and Characterization. Iron oxide (Fe_3O_4) nanoparticles coated with a copolymer of chitosan and PEG (NP) were used as the base NP in this study owing to their proven stability and biocompatibility. Amine functional NPs were tagged with Alexa Fluor 647 (AF647) for optical detection in *in vivo* experiments or Oregon Green 488 for *in vitro* detection. These optically detectible NPs were then activated with thiolated neu antibody[18] through a heterobifunctional PEG linker to display neu away from the surface of the NP, generating NP-neu. The structure of NP-neu is shown in Figure 1a. Mouse IgG was attached to NP to form NP-IgG as a control. The numbers of AF647 and antibodies per NP were calculated assuming a NP core size of 8 nm (Suppl. Figure 1, Supporting Information) and are provided in Table 1.

The size and zeta potential of NPs have a dramatic effect on nonspecific uptake by off-target cells in the body. After conjugation of antibodies, NPs slightly decreased in size which may be due to the additional purifications using size exclusion chromatography that could slowly remove the largest, and smallest, NPs. NP-IgG had a Z-average size of 44 $\pm$ 6 and NP-neu had a Z-average size of 40 $\pm$ 1 (Table 1), with small PdI values (Table 1) and narrow size distributions (Figure 1b) indicating monodispersity. The slight decrease in PdI values further suggests the decrease in the average hydrodynamic size of the NPs was due to additional purifications that removed the largest, and smallest, NPs. NPs between the sizes of 10−100 nm in diameter are desirable since they are too large to be filtered out by the kidneys but small enough to not be recognized by the reticuloendothelial system for elimination.[8,19] Furthermore, NPs smaller than 60 nm are expected to have better penetration away from blood vessels and into the tumor.[20]

The zeta potential, a measure of the surface charge on the NP, also plays a significant role in non-specific uptake and tumor targeting. After antibody attachment, NP-IgG and NP-neu had zeta potentials of −1.3 $\pm$ 1.3 mV and −0.4 $\pm$ 0.8 mV, respectively (Figure 1c and Table 1), similar to the zeta potential of unmodified NPs (Table 1). Although chitosan alone is slightly cationic (pK_a around 6.5), PEGylation and coating onto iron oxide NPs creates a near neutral NP. These near neutral zeta potentials are ideal for a targeted NP so that antibody−antigen binding will

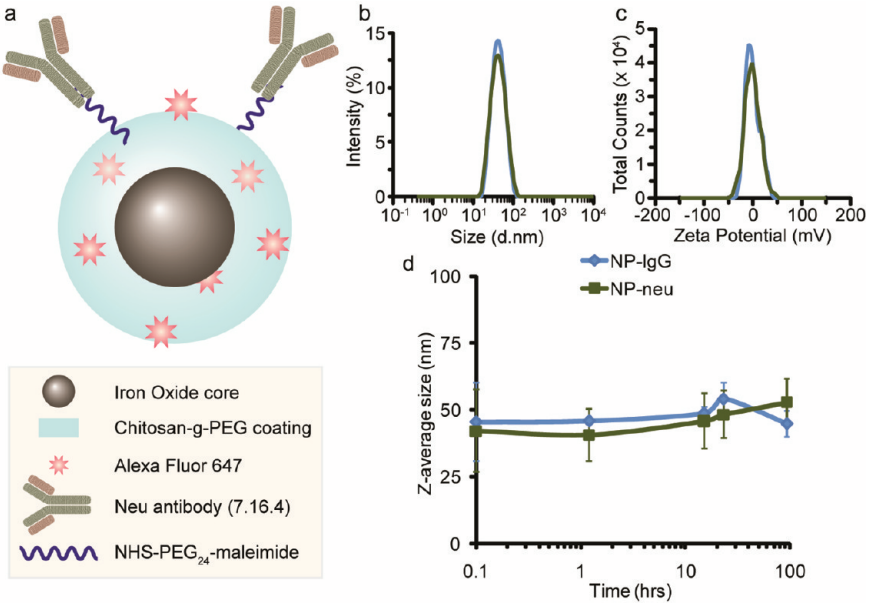

Figure 1. NP architecture and characterizations. (a) Illustration of the architecture of the fluorescently labeled and neu antibody-activated NP. (b) Hydrodynamic size distributions of NP-IgG and NP-neu as determined by DLS. (c) Zeta potential distributions of NP-IgG and NP-neu as determined by DLS. (d) SPION stability in biological fluid (DMEM containing 10% FBS).

TABLE 1. NP Characterizations

sample	AF-647 per NP[a]	Ab per NP[b]	Z-average (d.nm)[c]	PdI[d]	zeta potential (mV)
NP	0	0	47 ± 12	0.19 ± 0.03	−1.4 ± 1.5
NP-IgG	25 ± 3	8 ± 0. 5	44 ± 6	0.18 ± 0.08	−1.3 ± 1.3
NP-neu	25 ± 3	6 ± 2	40 ± 1	0.15 ± 0.06	−0.4 ± 0.8

All NP characterizations are provided as the average and standard deviation of five batches of NPs.

[a] The number of AF-647 per NP was determined by absorbance at 650 nm and calculated according to the manufacturer's (Invitrogen, Carlsbad, CA) protocol assuming a NP core diameter of 8 nm. [b] The number of antibodies per NP was determined by reducing SDS-PAGE and calculated assuming an antibody molecular weight of 150 kDa and NP core diameter of 8 nm. [c] Hydrodynamic Z-average diameter in nm. [d] Polydispersity index.

not be confounded by nonspecific electrostatic interactions. Highly cationic NPs are preferentially taken up by the liver[21] and show poor penetration into the tumor.[22] Slightly anionic NPs show the best tumor uptake and penetration.[21,22] However, highly anionic NPs can still nonspecifically interact with positively charged membrane-bound proteins. Therefore, neutral NPs are expected to provide the best targeting ability since nonspecific electrostatic interactions between the NP and off-target cells will be minimal. Furthermore, the similar sizes and zeta potentials of NP-neu and NP-IgG ensures any targeting role is solely due to the presence of the targeting antibody and not to the differences in physiochemical properties shown in Table 1.

NP stability is important to ensure NP targeting functionality. Aggregation of NPs can reduce targeting ability and increase uptake by the RES and the risk of embolism. The stability of NP-IgG and NP-neu were tested in DMEM containing 10% FBS (Figure 1d). Both NPs were stable for at least five days in culture medium and did not induce aggregation of erythrocytes (Suppl. Figure 2, Supporting Information) suggesting they should function well in targeting experiments and not risk embolism *in vivo*. Furthermore, previous experiments in mice showed high stability of these chitosan-grafted PEG coated NPs in whole blood as evidenced by a long serum half-life of 7−8 h.[23] Additionally, these NPs have proven nontoxicity[24,25] (Suppl. Figure 3 and Supplementary Results and Discussion, Supporting Information).

***In Vitro* Targeting.** To test the specific binding of NP-neu to the neu antigen on the surface of MMC cells, both target MMC cells and control MDA-MB-231 cells were treated with various AF647 labeled NP formulations including (1) NP-neu, (2) NP-IgG, and (3) either NP-neu or NP-IgG with an excess of free competing neu antibody. In the third situation, the free neu antibody competes for surface binding sites with NP-neu, so an excess of free neu antibody ensures most binding sites are not available for NP-neu binding. Since neu is an internalized antibody (Suppl. Figure 4, Supporting Information), NP-IgG was treated with excess free neu antibody to ensure the free antibody in solution did not promote nonspecific uptake of control NPs through increased endocytosis. NP labeling of target MMC and control MDA-MB-231 cells was analyzed by flow cytometry (Figure 2). NP-IgG showed little binding to MMC cells which was not affected by free neu in solution, whereas NP-neu provided significantly increased binding to MMC cells which was abrogated

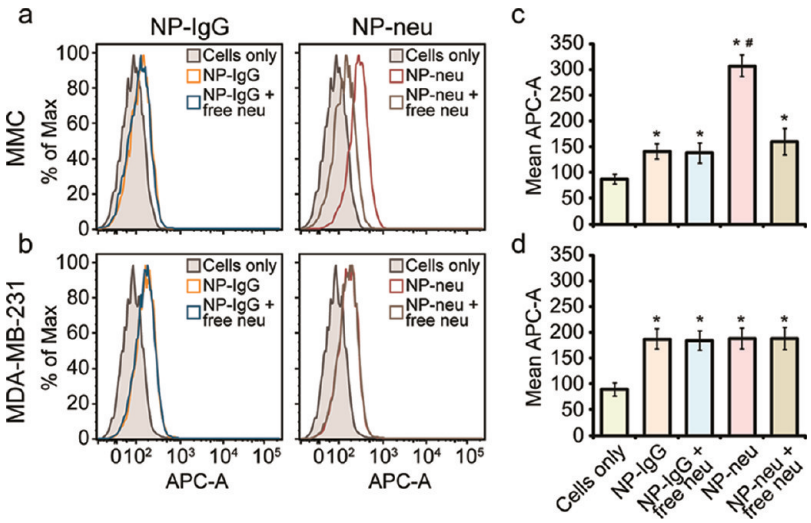

Figure 2. Flow cytometry analysis of NP labeling of breast cancer cells. (a) Histograms of AF647 fluorescence in target MMC cells treated with control NP-IgG and targeted NP-neu in the presence or absence of free neu. (b) Histograms of AF647 fluorescence in control MDA-MB-231 cells treated with control NP-IgG and targeted NP-neu in the presence or absence of free neu. (c) Quantification of AF647 fluorescence in target MMC cells treated with control NP-IgG and targeted NP-neu. (d) Quantification of AF647 fluorescence in control MDA-MB-231 cells treated with control NP-IgG and targeted NP-neu. * indicates a statistical significance as compared to untreated cells, # indicates a statistical significance as compared to NP-IgG control, $n = 3$ for each condition.

to background uptake when free neu was used (Figure 2a, c). This approximately 4-fold increase in cell labeling suggests that NP-neu selectively recognized the neu antigen on the surface of MMC cells. On the other hand, both NP-IgG and NP-neu provided similar cell labeling in control MDA-MB-231 cells, which was not affected by free neu in solution (Figure 2b, d). These data show the ability of NP-neu to selectively label target MMC cells through direct binding to the neu antigen on the surface of these cells.

To confirm NP labeling of target MMC cells, the iron uptake in treated cells was determined using the ferrozine assay (Figure 3). Untreated cells had little iron and there was a small amount of nonspecific uptake of NP-IgG by MMC cells. The cells treated with NP-neu had significantly greater iron content than those treated with NP-IgG, which was reduced to below background uptake through addition of free neu antibody in a competition assay. This 3-fold improvement, after accounting for baseline intracellular iron content, in NP uptake combined with free antibody competition tests further suggests that NP-neu is able to specifically target neu on the surface of MMC cells.

To further confirm the targeting and determine cellular localization of NP-neu, treated cells were imaged using confocal microscopy (Figure 4). Untreated cells showed no fluorescence as expected. Cells treated with NP-IgG showed minimal fluorescence as a result of the low nonspecific uptake of these NPs. Cells treated with NP-neu showed high labeling efficiency which was blocked by free neu if present, a result of the specific interaction of NP-neu with the neu receptor on these cells. The fluorescent signal from NP-neu treated cells was both colocalized with the cell membrane (yellow color) and in

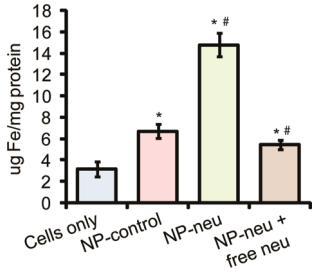

Figure 3. *In vitro* targeting of MMC cells. Iron in cells treated with NP-control, NP-neu, and NP-neu plus free neu was determined using the ferrozine assay ($n = 3$ for each condition). * indicates statistical significance as compared to cells only. # indicates statistical significance as compared to NP-control.

the perinuclear region (green color around the nucleus), which suggested receptor-mediated endocytosis.[26] The specific targeting and intracellular accumulation of neu (Suppl. Figure 4, Supporting Information) shows this neu labeled NP should function well as a breast cancer targeting agent for *in vivo* imaging, if labeled with an appropriated near-infrared fluorophore, and drug delivery, through conjugation of drugs to available amine groups on the surface of the NP. The internalization of NP-neu by target cells increases the likelihood of the delivered therapy reaching its intracellular site of action. The near-neutral charge of the NP along with the biocompatible chitosan-g-PEG coating provides a highly stable NP that shows minimal nonspecific interaction with cells. These properties are ideal for a targeting NP where the specific interaction between the targeting agent and cell surface receptor must far outweigh any nonspecific electrostatic or hydrophobic interactions or surface energy induced aggregation or binding.

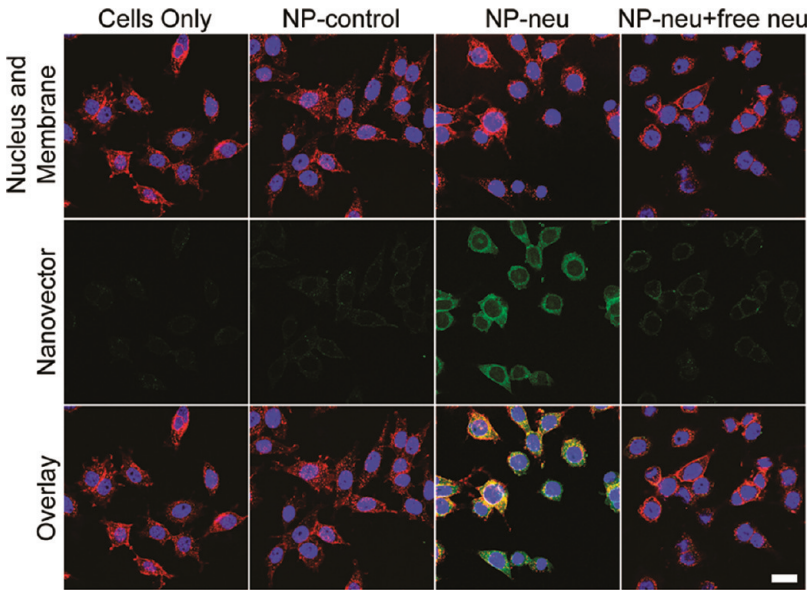

Figure 4. Confocal imaging of NP treated MMC cells. Cells were treated with nontargeted NP-control, targeted NP-neu, or targeted NP-neu with excess free neu for 2 h in fully supplemented culture media. The images of untreated cells (first column) are provided as a reference. Bright green fluorescence is only seen in the NP-neu treated cells indicating these NPs are able to target the neu receptor on neu expressing cells. Image acquisition times were identical for all the samples. Scale bar corresponds to 20 μm.

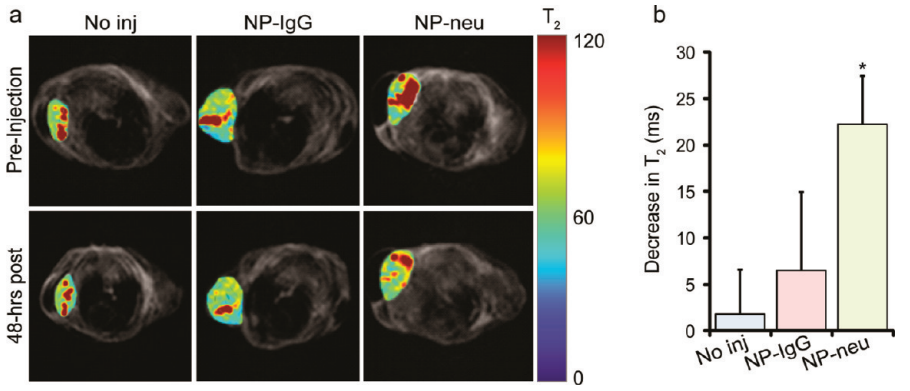

Figure 5. MRI of NP treated transgenic breast cancer mice. (a) Colorized T_2 maps of the tumor site were overlaid onto anatomical images. Noninjected and control NP-IgG injected mice showed no significant T_2 changes in their tumors 48 h postinjection. Targeted NP-neu treated mice showed shortened T_2 relaxation times in tumors 48 h postinjection, indicating that there was a significant uptake of NPs. (b) Decrease in T_2 relaxation times 48 h after injection. A much larger decrease in T_2 relaxation time was observed in tumors of NP-neu treated mice (n = 3) as compared to no injection (n = 2) than NP-IgG (n = 3), suggesting a targeting role of NP-neu. * indicates a statistical difference as compared to no injection.

MRI of neu Transgenic Mice. The ability of NP-neu to target metastatic breast cancer and be detected in MRI was tested in transgenic mice. T_2 maps were generated for mice injected with NPs and the tumor region overlaid on anatomical images (Figure 5a). The dark regions in the anatomical images correspond to the lungs as the early developing tumors were located in the anterior mammary tissue, near the front legs. Uninjected mice showed no change in T_2 relaxation time in the tumor region between preinjection and 48 h postinjection. Mice injected with nontargeted NP-IgG showed a small shortening in T_2 relaxation time 48 h after injection as a result of nonspecific uptake into the tumor through the enhanced permeability and retention (EPR) effect. The tumors from mice injected with targeted NP-neu showed a significant shortening in T_2 relaxation time which reveals the ability of NP-neu to provide contrast enhancement in MRI for disease detection or monitoring of drug delivery. Furthermore, the contrast enhancement 48 h after injection reveals the ability of NP-neu to persist in the tumor at a detectable level for a significant period of time which is useful for response monitoring. The decreases in T_2 relaxation time from the preinjection to 48 h postinjection were quantified for all mice and are provided in Figure 5b. This quantification shows the insignificant change in T_2 relaxation time over 48 h in uninjected mice (n = 2), and provides a detection limit for the SPIONs since SPION concentrations that shorten T_2 by less than approximately 6 ms would not be detected

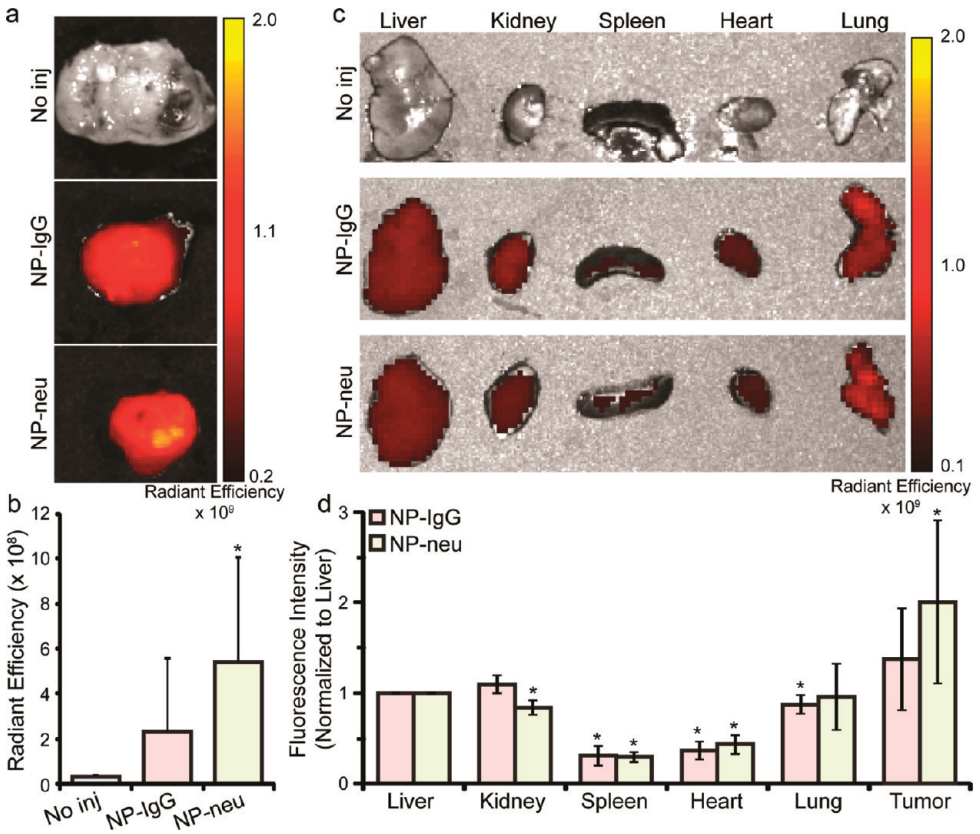

Figure 6. Xenogen imaging of harvested tumors and organs from transgenic breast cancer mice. (a) Higher fluorescence intensity can be observed in tumors from NP-neu (targeted) treated mice than from NP-IgG (control) treated mice. (b) Fluorescence intensities (photons/sec/cm^2/steradian)/(μW/cm^2) of tumors from mice left untreated (n = 5) or treated with NP-IgG (n = 5 tumors) or NP-neu (n = 7 tumors). * indicates a statistical difference as compared to no injection. (c) Xenogen images of livers, kidneys, spleens, hearts, and lungs from uninjected, NP-IgG injected (control, n = 3), and NP-neu injected (targeted, n = 5) mice. (d) Liver normalized fluorescence quantification of organs indicating nonspecific uptake was similar for both NP-IgG and NP-neu, and uptake in tumors was higher than in off-target organs. * indicates a statistical difference from liver uptake.

over background in these mice. This corresponds to a tumor concentration of approximately 6 μg/mL assuming a relaxivity of 100 s^{-1} mM^{-1} at 3T. In the clinic, the minimal SPION concentration would have to be determined from precontrast MRI images and based on the noise between images. T_2 values in tumors from NP-IgG injected mice (n = 3) decreased slightly, and decreased significantly in tumors from NP-neu treated mice (n = 3). The slight, but insignificant, contrast enhancement in NP-IgG injected mice was likely due to the nonspecific uptake through the EPR effect which had not yet cleared out. On the other hand, NP-neu specifically bound to breast cancer cells and thus remained in the tumor to provide significant contrast enhancement as compared to uninjected mice. Similar results have been observed using xenograft mouse models where the targeting moiety on the surface of the NP promotes cell uptake and distribution throughout the tumor.[27−31]

***Ex Vivo* Fluorescence Imaging.** Mice were sacrificed and dissected to remove tumors, livers, spleens, kidneys, lungs, and hearts 48 h after NP injections. Organs were then imaged using an IVIS Xenogen imaging system which detects the AF647 tag on the NPs. Figure 6a shows representative tumors from mice receiving no injection, NP-IgG injection, and NP-neu injection. Mice receiving no injection showed no fluorescence as expected. Tumors from mice treated with NP-IgG and NP-neu showed fluorescent signal with NP-neu treated tumors appearing brighter than NP-IgG treated tumors. Similarly to MRI analysis, tumors from NP-IgG treated mice did not show a statistically significant increase in fluorescence as compared to uninjected mice (p = 0.22) whereas tumors from NP-neu treated mice showed a statistically significant increase in fluorescence as compared to uninjected mice (p = 0.04). Fluorescence intensity (average radiant efficiency) was quantified in tumors from NP-IgG and NP-neu injected mice and normalized to liver intensity to account for any confounding factors between animals. Figure 6b shows the liver normalized fluorescence intensity where tumors from NP-neu treated mice were consistently brighter than tumors from NP-IgG treated mice. This further suggests a targeting role of NP-neu in breast cancer even though improvement in NP-neu uptake *in vivo* was not as significant as *in vitro*. This is not unexpected and is consistent with current literature indicating the targeting agent attached to NPs does

not significantly increase accumulation in the tumor but improves uptake and retention in tumor cells.[27−31] The EPR effect promotes the accumulation of both targeted and nontargeted NPs into the tumor site, but only targeted NPs selectively bind to, or are taken up by, tumor cells.

To examine nonspecific binding of NPs, the livers, kidneys, spleens, lungs, and hearts from treated mice were imaged using the Xenogen imaging system. Figure 6c shows representative images of organs, which shows that the nonspecific uptake of NPs was the same for both control NP-IgG and targeted NP-neu. Figure 6d shows the liver normalized fluorescent signal (original liver fluorescence signal was $1.7 \times 10^8 \pm 1.65 \times 10^8$ (photons/sec/cm^2/steradian)/(μW/cm^2) for NP-IgG and $2.24 \times 10^8 \pm 1.36 \times 10^8$ (photons/sec/cm^2/steradian)/(μW/cm^2) for NP-neu) from the organs confirming no statistical different in off-target uptake between control NP-IgG and targeted NP-neu. The hearts and spleens of treated animals had significantly lower NP uptake than the liver and were not affected by targeting. The kidneys from NP-neu treated mice and lungs from NP-IgG treated mice had slightly lower uptake of NPs than liver. These off-target results indicate the improved tumor uptake achieved by NP-neu was specific and not due higher nonspecific interaction with cells. Furthermore, the uptake in the tumors was higher than in off-target organs including the liver, and almost 2-fold higher for NP-neu. This is likely a result of the long serum half-life of these chitosan-grafted PEG coated NPs[23] and indicates their optimal size and neutral charge to avoid elimination by the kidneys and liver and sufficient passivation to prevent immune recognition.

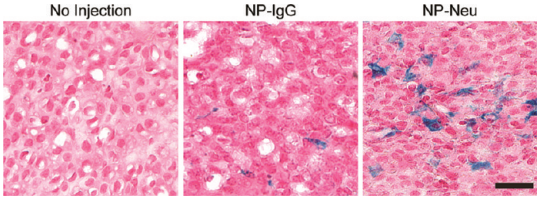

Figure 7. Histology images of tumors from NP treated transgenic breast cancer mice 48 h postinjection. Iron was stained using Prussian blue, and nuclei were counterstained with nuclear fast red. NP uptake in tumors from NP-neu (targeted) treated mice was much more pronounced and broadly distributed than the uptake in tumors of NP-IgG (control) treated mice. Scale bar corresponds to 20 μm.

Tumor Histology. To observe distribution of NPs within the tumor, tumor sections were stained with Prussian blue to detect iron from NPs and counterstained with nuclear fast red (Figure 7). Tumors from mice treated with NP-neu showed significant iron staining distributed throughout the tumor whereas those from mice treated with NP-IgG showed little, isolated iron staining. Tumors from untreated mice showed no positive iron staining. This further suggests the targeting ability of NP-neu toward the breast cancer cells. Furthermore, this highlights the importance of a targeting agent for breast cancer diagnosis and therapy, as a larger proportion of cells are exposed to the injected NP-neu as a result of targeting, increasing the efficiency of an attached therapeutic agent.

Targeting Micrometastases. It is important to detect and treat metastatic disease as this is the most common cause of cancer mortality. In fact, 90% of cancer-related mortality is caused by metastases.[3−5] The transgenic mice used in this study are known to develop lung, liver, and bone marrow metastases within 8 months and thus are an excellent model for targeting metastases.[32−34] To observe targeting of breast cancer metastases, lungs and livers from treated mice were sectioned and stained identically to the primary tumors (Figure 8). Positive Prussian blue staining in the lung and liver metastases indicates the presence of NPs.[35,36] Micrometastases in lungs and

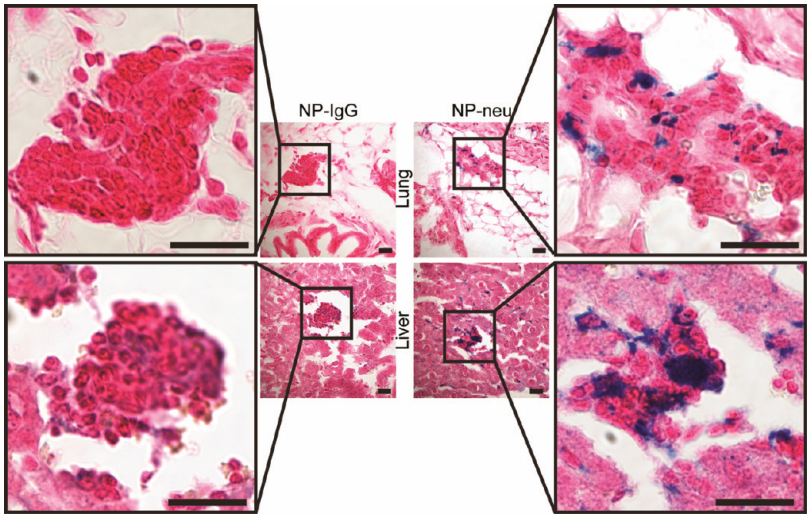

Figure 8. Prussian blue stained histology images of micrometastases in lungs and livers from NP-IgG (control) and NP-neu (targeted) treated transgenic breast cancer mice. Scale bars correspond to 20 μm.

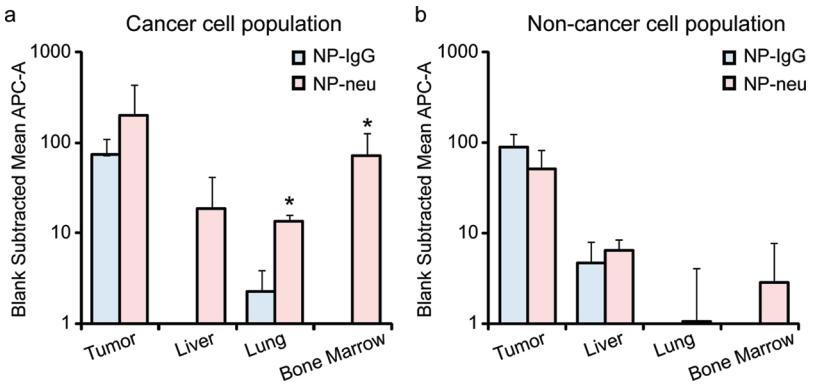

Figure 9. Flow cytometry analysis of NP uptake in metastatic cancer cells and organs. (a) NP fluorescence in the cancer cell population from the primary tumor, liver, lung, and bone marrow of NP-IgG and NP-neu treated mice. Higher fluorescence was observed in double positive metastatic cancer cells in all tested organs from mice treated with NP-neu as compared to NP-IgG. (b) NP fluorescence in the noncancer cell population from the primary tumor, liver, lung, and bone marrow of NP-IgG and NP-neu treated mice. Similar fluorescence levels were observed between NP-neu and NP-IgG treated animals. Fluorescence intensities were normalized by subtracting the background fluorescence of cells from untreated mice to allow for direct comparison between treatment groups and cell types. * indicates a statistical significance as compared to NP-IgG.

livers from mice treated with control NP-IgG showed no positive iron staining. On the other hand, lung and liver micrometastases from NP-neu treated mice showed significant positive iron staining. This targeting effect on micrometastases by NP-neu was further confirmed using flow cytometry analysis of NP fluorescence in CD44-Integrin-α6 (CD49f) double positive metastatic cells[37,38] (Figure 9a, Suppl. Table 1, Supporting Information). Little to no labeling of metastatic cells in the lungs and livers from NP-IgG treated mice was observed, whereas there was dramatically higher NP fluorescence in NP-neu treated mice. Furthermore, metastatic cancer cells in aspirated bone marrow were successfully labeled with NP-neu as compared to NP-IgG ($p = 0.05$, $n = 3$). This demonstrates the ability of these NPs to selectively detect and label early stage micrometastases, but imaging was only possible through histology or flow cytometry and not MRI since the micrometastases were beyond the spatial resolution of 3T MRI. Flow cytometry analysis also revealed the nonspecific uptake of NPs in noncancerous cells (Figure 9b). Again, we saw no significant difference between the nonspecific uptake of NP-IgG and NP-neu in off-target cells showing the specificity of NP-neu. Also, the NP uptake in the tumor cells was higher than NP uptake in noncancerous liver cells as seen in Figure 6d. Furthermore, there was much lower uptake of NP-neu in noncancerous cells as compared to metastatic cells in these tissues, whereas uptake of NP-IgG was similar between cancerous and noncancerous cells.

Targeting of micrometastases was much more pronounced than primary tumor targeting when comparing targeted (NP-neu) and nontargeted (NP-IgG) NPs, which is likely due to the lack of the EPR effect in early stage micrometastases. Large tumors contain leaky vasculature allowing large influx of blood including nutrients and oxygen, and have insufficient lymph vessels to remove waste. This leads to the EPR effect which can be used for passive targeting of tumors with NPs. However, micrometastases, which can currently only be identified histologically, are still small enough where diffusion provides adequate oxygen,[39] so tumor angiogenesis is not yet induced by anoxic conditions. Unlike the large tumors, lymphatic drainage from the lungs and liver, and hepatic ducts of the liver, are adequate to remove waste. Therefore, these metastases do not have the enhanced retention associated with large tumors and thus cannot be passively targeted. This explains why a more significant targeting effect was seen in these metastases by targeted delivery; NP-neu attached to breast cancer cells through specific interaction with neu expressed on the cell surface, and NP-IgG was likely removed through lymphatic or hepatic drainage. This further confirms the targeting role of NP-neu and highlights the critical need for targeted delivery especially for metastatic disease.

CONCLUSIONS

Rationally designed superparamagnetic iron oxide NPs activated with an antibody against the neu receptor were successfully prepared. These NPs were able to specifically target neu expressing mouse mammary carcinoma cells *in vitro* and *in vivo* in a transgenic mouse model and were detected with MRI. Furthermore, these NPs were able to recognize and tag spontaneous micrometastases in the lungs, livers, and bone marrow of these mice indicating the potential for MRI detection of micrometastases. Control NPs showed no labeling of metastatic cells highlighting the importance of targeting for delivery to metastatic disease. Given that these NPs have a significant number of functional groups, therapeutic payloads such as small molecule chemotherapy drugs, DNA, or siRNA could be attached for targeted therapy. The favorable properties

displayed by this SPION system in a transgenic mouse model warrants its further development as a diagnostic tool for metastatic breast cancer, and as a therapeutic agent to significantly improve the prognosis of patients afflicted with metastatic breast cancer.

METHODS

NP Synthesis. SPIONs (Fe_3O_4) coated with a copolymer of chitosan-g-PEG were synthesized *via* a coprecipitation method as previously described.[25] Briefly here, chitosan oligosaccharide (5 kDa) was PEGylated with aldehyde-activated methoxy PEG (2 kDa), and monolabeled chitosan-g-PEG (CP) was purified using ion exchange chromatography. Pure CP (150 mg) was mixed with iron chlorides (9.3 mg Fe^{2+} and 16 mg Fe^{3+}) in 2.2 mL of degassed deionized water. A 15% ammonium hydroxide solution (1.2 mL) was titrated in slowly at 40 °C until a final pH of 10 was reached to ensure complete nucleation of NPs. NPs were purified through size exclusion chromatography in S-200 resin (GE Healthcare, Piscataway, NJ) into thiolation buffer (100 mM sodium bicarbonate buffer, pH 8.0 containing 5 mM EDTA). Synthesized NPs contained approximately 150 CPs per iron core which provided free amine groups for subsequent conjugations as determined by the fluorescamine assay.

NP Conjugations. Monoclonal antibody specific to the transgenic rat neu (7.16.4) expressed by the MMC cells and FVB/N transgenic mouse model used in this study was purchased from the UCSF Monoclonal Antibody Core. Mouse IgG (Invitrogen, Carlsbad, CA) was used as a control. Antibodies (2.5 mg/mL in thiolation buffer) were thiolated with Traut's reagent (100 μg/mL in thiolation buffer) by mixing 874 μL antibody with 25 μL Traut's reagent for 1.5 h in the dark at room temperature. Unreacted Traut's reagent was removed through Zeba spin columns (Thermo Fisher Scientific, Rockford, IL). Concurrently, NPCP were labeled with Alexa Fluor 647 (AF647, Invitrogen, Carlsbad, CA). NPCP (1.1 mg in 1 mL thiolation buffer) were reacted with 0.5 mg of AF647 in 100 μL DMSO for 1 h at room temperature protected from light with gentle rocking. For *in vitro* confocal imaging experiments, NPCP were labeled with Oregon Green 488 (1.1 mg NP in 1 mL thiolation buffer, 0.25 mg Oregon Green 488 in 100 μL DMSO). Unreacted fluorophore was removed using S-200 resin and pure NPCP-fluorophore was collected. NPCP-fluorophore was reacted with 9.5 μL of 2.5 mM NHS-PEG_{24}-maleimide in the dark at room temperature with gentle rocking for 15 min before removing unreacted PEG through PD-10 desalting columns (GE Healthcare, Piscataway, NJ). The thiolated antibodies were mixed with thiol-reactive NPs (2 mg antibody per 1 mg NPs) and allowed to react for 4 h in the dark at room temperature with gentle rocking. Unreacted antibody was removed from NP conjugated antibodies through size exclusion chromatography in S-200 resin to have pure control NP-IgG and targeted NP-neu.

NP-Antibody Characterizations. The size and zeta potential of NP-IgG and NP-neu were determined using a DTS Zetasizer Nano (Malvern Instruments, Worcestershire, U.K.) by measuring dynamic light scattering of a 100 μg/mL suspension of NPs at pH 7.4. The stability of NPs were determined at 100 μg/mL in DMEM containing 10% FBS and 1% antibiotic-antimycotic. AF647 labeling of NPCP was determined through absorbance measurement at 650 nm using unlabeled NPCP as a background. Molar concentration of AF647 was calculated following the manufacturer's protocol, and the number of AF647 per NPCP was calculated assuming a NP core diameter of 8 nm (see Supplementary Methods for detailed description, Supporting Information). Antibody loading on NPs was determined through reducing SDS-PAGE and quantifying the amount of light chain released from NPs (see Supplementary Methods for detailed description). The number of antibodies per NP was calculated assuming an antibody molecular weight of 150 kDa and a NP core diameter of 8 nm (see Supplementary Methods for detailed description).

***In Vitro* Targeting.** Mouse mammary carcinoma (MMC) cells that express rat transgenic neu were maintained at 37 °C in 95%/5% humidified air/CO_2 in DMEM containing 10% FBS and 1% antibiotic-antimycotic. For targeting experiments, 50000 cells were plated in 24-well plates the day before NP treatment. NP treatments were performed in fully supplemented culture medium at 50 μg/mL NPs. For the competition treatment, cells were treated with 50-fold excess free neu antibody for 15 min before adding NP-neu. After a 2 h treatment, cells were washed thrice before preparation for detection of NP labeling. For fluorescence detection, cells were detached using Versene (Invitrogen, Carlsbad, CA) and collected in FACS buffer (2% FBS in PBS). Cell uptake of NPs was determined by flow cytometry detection of AF647 fluorescence of at least 10000 cells on a BD FACSCanto flow cytometer (Beckton Dickinson, Franklin Lakes, NJ). Data was analyzed using the FlowJo software package (Tree Star, Ashland, OR). For iron detection, the ferrozine assay was used as previously described[40] and iron content was normalized to protein content using Bradford (see Supplementary Methods for a more detailed description of the assay, Supporting Information).

Confocal Imaging. MMC cells (500000) were plated on 22 × 22 mm glass coverslips in 6-well plates the day before NP treatment. Cells were treated with NPs as described above before fixing in 4% methanol-free formaldehyde (Polysciences Inc., Warrington, PA) for 15 min. Cell membranes were stained with wheat germ agglutinin, Alexa Fluor conjugates (Invitrogen, Carlsbad, CA) following the manufacturer's protocol. Coverslips were then mounted on microscope slides using Prolong Gold antifade solution (Invitrogen, Carlsbad, CA) containing DAPI for cell nuclei staining. Cell images were obtained on a LSM 510 Meta confocal fluorescence microscope (Carl Zeiss Inc., Peabody, MA) with the appropriate filters (see Supporting Information for detailed procedures).

***In Vivo* MRI.** All animal experiments were performed in accordance with the University of Washington Internal Animal Care and Use Committee (IACUC). Transgenic mice (FVB/N/Tg) which are homozygous for the mouse mammary tumor virus (MMTVneu) rat transgene and spontaneously form mammary tumors were purchased from The Jackson Laboratory (Sacramento, CA) and bred in-house. Mice were used for experiments after palpable tumors developed. For precontrast MR imaging, mice were anesthetized with isofluorane and placed into a 4-mouse holder fit for a knee-coil and maintained at 35 °C with heated air. Imaging was conducted on a Philips Achieva 3T Whole Body Scanner (Philips Medical Systems, Andover, MA). A series of T_2 weighted axial images were generated by using a single echo multislice pulse sequence with a T_R of 8004 ms and variable T_E values from 40 to 420 ms in 20 ms increments. The spatial resolution parameters were as follows: acquisition matrix of 512 × 512, field of view of 75 × 75 mm, slice number of 15, slice thickness of 2 mm, gap thickness of 2 mm, and 2 averages for T_2 weighted images. Mice were then injected with a single bolus containing 200 μL of 522 μg/mL NP-IgG or NP-neu intravenously through the tail vein using a 27-gage needle. Postcontrast MR imaging was then performed 48 h after injection for uninjected ($n = 2$), NP-IgG injected ($n = 3$), and NP-neu injected ($n = 3$) mice. Colorized T_2 maps were generated using the OsiriX open-source software package and the manually selected tumor region was overlaid onto anatomical images. Average T_2 values over the manually selected tumor regions were used to calculate ΔT_2 (average precontrast T_2 − average postcontrast T_2). The volumes of the manually selected regions for tumors from uninjected, NP-IgG treated, and NP-neu treated mice were 120 ± 74 mm^3, 75 ± 27 mm^3, and 91 ± 15 mm^3, respectively.

***Ex Vivo* Imaging.** Anesthetized mice were euthanized through cervical dislocation 48 h postinjection. Mice were dissected to remove tumors, livers, kidneys, spleens, hearts, and lungs which were placed into 10% Formalin. Fluorescence from each organ was imaged using the IVIS Spectrum imaging system (Caliper Life Sciences, Hopkinton, MA) with the Living Image software package. Imaging conditions consisted of a high lamp level, excitation and emission wavelengths of 640 and 680 nm, respectively, f-stop at f4, and 1 s exposure time.

Histology. Formalin fixed tissues were placed into 30% sucrose at 4 °C until tissues sank. Tissues were then embedded in OCT compound and frozen. Frozen 4 μm sections were stained with Prussian blue for iron detection and counterstained with nuclear fast red. Stained sections were imaged using an upright Nikon Eclipse E600 microscope (Nikon Instruments, Melville, NY) and QImaging Retigia EX cooled CCD camera (QImaging, Surrey, BC, Canada).

***In Vivo* Flow Cytometry.** Anesthetized mice were euthanized through cervical dislocation 48 h postinjection. Mice were dissected to remove tumors, livers, brains, and femurs. Organs were placed into a collagenase solution (1% collagenase in PBS) on ice for 30 min and femurs were cleaned of all muscle and bone marrow aspirated with serum free DMEM medium. Organs were disaggregated through gentle pipetting with a wide pore pipet tip and tissue aggregates were removed through filtration with a 70 μm pore cell strainer (BD Biosciences, Franklin Lakes, NJ). Single cell suspensions of organs and bone marrow were then centrifuged at 300× *g* and the cell pellets resuspended into ACK buffer (150 mM ammonium chloride, 10 mM potassium bicarbonate, 0.1 mM EDTA) to lyse erythrocytes. Cells were washed thrice in ACK buffer until erythrocytes were completely removed. Cells were then stained with FITC conjugated anti-CD44 and PE conjugated anti-integrin alpha 6 (Abcam, Cambridge, MA) to identify the tumor cell population.[37,38] Cells were then analyzed on a BD FACSCanto flow cytometer (Beckton Dickinson, Franklin Lakes, NJ). Data was analyzed using the FlowJo software package (Tree Star, Ashland, OR).

Statistical Analysis. All acquired data are expressed as mean ± SD. Statistical significance was determined using Student's *t*-test. A *p*-value less than 0.05 was considered statistically significant.

Conflict of Interest: The authors declare no competing financial interest.

Acknowledgment. This work was supported in part by NIH grants R01CA134213 and R01EB006043. F.K., O.V., and V.L. acknowledge support from NIH training grant T32CA138312. We thank the Diagnostic Imaging Sciences Center, Animal Bioimaging Center, and Keck Microscopy Imaging Facility at the University of Washington for use of resources and equipment. We acknowledge the assistance of E. Gad and L. Rastetter for maintaining and providing transgenic mice. We also thank J. Phillips and D. Cheung for laboratory assistance.

Supporting Information Available: TEM images of NP cores, erythrocyte aggregation assay, z-stack confocal imaging, and detailed procedures. This material is available free of charge *via* the Internet at http://pubs.acs.org.

REFERENCES AND NOTES

1. Jemal, A.; Siegel, R.; Ward, E.; Hao, Y.; Xu, J.; Thun, M. J. Cancer Statistics, 2009. *CA Cancer J. Clin.* **2009**, *59*, 225–249.
2. Altekruse, S.; Kosary, C.; Krapcho, M.; Neyman, N.; Aminou, R.; Waldron, W.; Ruhl, J.; Howlader, N.; Tatalovich, Z.; Cho, H.; *et al.* Seer Cancer Statistics Review, 1975−2007. *Natl. Cancer Inst.* **2010**.
3. Weigelt, B.; Peterse, J. L.; van 't Veer, L. J. Breast Cancer Metastasis: Markers and Models. *Nat. Rev. Cancer* **2005**, *5*, 591–602.
4. Mehlen, P.; Puisieux, A. Metastasis: A Question of Life or Death. *Nat. Rev. Cancer* **2006**, *6*, 449–458.
5. Ma, L.; Reinhardt, F.; Pan, E.; Soutschek, J.; Bhat, B.; Marcusson, E. G.; Teruya-Feldstein, J.; Bell, G. W.; Weinberg, R. A. Therapeutic Silencing of miR-10b Inhibits Metastasis in a Mouse Mammary Tumor Model. *Nat. Biotechnol.* **2010**, *28*, 341–347.
6. Kievit, F. M.; Zhang, M. Cancer Nanotheranostics: Improving Imaging and Therapy by Targeted Delivery across Biological Barriers. *Adv. Mater.* **2011**, *23*, H217–247.
7. Hao, R.; Xing, R.; Xu, Z.; Hou, Y.; Gao, S.; Sun, S. Synthesis, Functionalization, and Biomedical Applications of Multifunctional Magnetic Nanoparticles. *Adv. Mater.* **2010**, *22*, 2729–2742.
8. Veiseh, O.; Gunn, J. W.; Zhang, M. Design and Fabrication of Magnetic Nanoparticles for Targeted Drug Delivery and Imaging. *Adv. Drug Deliv. Rev.* **2010**, *62*, 284–304.
9. Rouzier, R.; Perou, C. M.; Symmans, W. F.; Ibrahim, N.; Cristofanilli, M.; Anderson, K.; Hess, K. R.; Stec, J.; Ayers, M.; Wagner, P.; *et al.* Breast Cancer Molecular Subtypes Respond Differently to Preoperative Chemotherapy. *Clin. Cancer Res.* **2005**, *11*, 5678–5685.
10. Parker, J. S.; Mullins, M.; Cheang, M. C.; Leung, S.; Voduc, D.; Vickery, T.; Davies, S.; Fauron, C.; He, X.; Hu, Z.; *et al.* Supervised Risk Predictor of Breast Cancer Based on Intrinsic Subtypes. *J. Clin. Oncol.* **2009**, *27*, 1160–1167.
11. Colombo, M.; Corsi, F.; Foschi, D.; Mazzantini, E.; Mazzucchelli, S.; Morasso, C.; Occhipinti, E.; Polito, L.; Prosperi, D.; Ronchi, S.; *et al.* HER2 Targeting as a Two-Sided Strategy for Breast Cancer Diagnosis and Treatment: Outlook and Recent Implications in Nanomedical Approaches. *Pharmacol. Res.* **2010**, *62*, 150–165.
12. Slamon, D. J.; Leyland-Jones, B.; Shak, S.; Fuchs, H.; Paton, V.; Bajamonde, A.; Fleming, T.; Eiermann, W.; Wolter, J.; Pegram, M.; *et al.* Use of Chemotherapy Plus a Monoclonal Antibody against HER2 for Metastatic Breast Cancer That Overexpresses HER2. *N. Engl. J. Med.* **2001**, *344*, 783–792.
13. Mazzucchelli, S.; Colombo, M.; De Palma, C.; Salvade, A.; Verderio, P.; Coghi, M. D.; Clementi, E.; Tortora, P.; Corsi, F.; Prosperi, D. Single-Domain Protein A-Engineered Magnetic Nanoparticles: Toward a Universal Strategy to Site-Specific Labeling of Antibodies for Targeted Detection of Tumor Cells. *ACS Nano* **2010**, *4*, 5693–5702.
14. Xu, C.; Wang, B.; Sun, S. Dumbbell-Like Au-Fe3o4 Nanoparticles for Target-Specific Platin Delivery. *J. Am. Chem. Soc.* **2009**, *131*, 4216–4217.
15. Dilnawaz, F.; Singh, A.; Mohanty, C.; Sahoo, S. K. Dual Drug Loaded Superparamagnetic Iron Oxide Nanoparticles for Targeted Cancer Therapy. *Biomaterials* **2010**, *31*, 3694–3706.
16. Singh, A.; Dilnawaz, F.; Mewar, S.; Sharma, U.; Jagannathan, N. R.; Sahoo, S. K. Composite Polymeric Magnetic Nanoparticles for Co-Delivery of Hydrophobic and Hydrophilic Anticancer Drugs and MRI Imaging for Cancer Therapy. *ACS Appl. Mater. Interfaces* **2011**, *3*, 842–856.
17. Sharpless, N. E.; Depinho, R. A. The Mighty Mouse: Genetically Engineered Mouse Models in Cancer Drug Development. *Nat. Rev. Drug Discovery* **2006**, *5*, 741–754.
18. Steinhauser, I.; Spankuch, B.; Strebhardt, K.; Langer, K. Trastuzumab-Modified Nanoparticles: Optimisation of Preparation and Uptake in Cancer Cells. *Biomaterials* **2006**, *27*, 4975–4983.
19. Alexis, F.; Pridgen, E.; Molnar, L. K.; Farokhzad, O. C. Factors Affecting the Clearance and Biodistribution of Polymeric Nanoparticles. *Mol. Pharm.* **2008**, *5*, 505–515.
20. Popovic, Z.; Liu, W.; Chauhan, V. P.; Lee, J.; Wong, C.; Greytak, A. B.; Insin, N.; Nocera, D. G.; Fukumura, D.; Jain, R. K.; *et al.* A Nanoparticle Size Series for *in Vivo* Fluorescence Imaging. *Angew. Chem., Int. Ed.* **2010**, *49*, 8649–8652.
21. Xiao, K.; Li, Y.; Luo, J.; Lee, J. S.; Xiao, W.; Gonik, A. M.; Agarwal, R. G.; Lam, K. S. The Effect of Surface Charge on *in Vivo* Biodistribution of PEG-Oligocholic Acid Based Micellar Nanoparticles. *Biomaterials* **2011**, *32*, 3435–3446.
22. Kim, B.; Han, G.; Toley, B. J.; Kim, C. K.; Rotello, V. M.; Forbes, N. S. Tuning Payload Delivery in Tumour Cylindroids Using Gold Nanoparticles. *Nat. Nanotechnol.* **2010**, *5*, 465–472.
23. Lee, M. J.; Veiseh, O.; Bhattarai, N.; Sun, C.; Hansen, S. J.; Ditzler, S.; Knoblaugh, S.; Lee, D.; Ellenbogen, R.; Zhang, M.; *et al.* Rapid Pharmacokinetic and Biodistribution Studies

Using Cholorotoxin-Conjugated Iron Oxide Nanoparticles: A Novel Non-Radioactive Method. *PLoS ONE* **2010**, *5*, e9536.
24. Kievit, F. M.; Veiseh, O.; Bhattarai, N.; Fang, C.; Gunn, J. W.; Lee, D.; Ellenbogen, R. G.; Olson, J. M.; Zhang, M. Q. Pei-Peg-Chitosan-Copolymer-Coated Iron Oxide Nanoparticles for Safe Gene Delivery: Synthesis, Complexation, and Transfection. *Adv. Funct. Mater.* **2009**, *19*, 2244–2251.
25. Veiseh, O.; Sun, C.; Fang, C.; Bhattarai, N.; Gunn, J.; Kievit, F.; Du, K.; Pullar, B.; Lee, D.; Ellenbogen, R. G.; *et al.* Specific Targeting of Brain Tumors with an Optical/Magnetic Resonance Imaging Nanoprobe across the Blood-Brain Barrier. *Cancer Res.* **2009**, *69*, 6200–6207.
26. Veiseh, O.; Sun, C.; Gunn, J.; Kohler, N.; Gabikian, P.; Lee, D.; Bhattarai, N.; Ellenbogen, R.; Sze, R.; Hallahan, A.; *et al.* Optical and MRI Multifunctional Nanoprobe for Targeting Gliomas. *Nano Lett.* **2005**, *5*, 1003–1008.
27. Kirpotin, D. B.; Drummond, D. C.; Shao, Y.; Shalaby, M. R.; Hong, K.; Nielsen, U. B.; Marks, J. D.; Benz, C. C.; Park, J. W. Antibody Targeting of Long-Circulating Lipidic Nanoparticles Does Not Increase Tumor Localization but Does Increase Internalization in Animal Models. *Cancer Res.* **2006**, *66*, 6732–6740.
28. Bartlett, D. W.; Su, H.; Hildebrandt, I. J.; Weber, W. A.; Davis, M. E. Impact of Tumor-Specific Targeting on the Biodistribution and Efficacy of Sirna Nanoparticles Measured by Multimodality *in Vivo* Imaging. *Proc. Natl. Acad. Sci. U.S.A.* **2007**, *104*, 15549–15554.
29. Wang, X.; Li, J.; Wang, Y.; Cho, K. J.; Kim, G.; Gjyrezi, A.; Koenig, L.; Giannakakou, P.; Shin, H. J.; Tighiouart, M.; *et al.* Hft-T, a Targeting Nanoparticle, Enhances Specific Delivery of Paclitaxel to Folate Receptor-Positive Tumors. *ACS Nano* **2009**, *3*, 3165–3174.
30. Choi, C. H.; Alabi, C. A.; Webster, P.; Davis, M. E. Mechanism of Active Targeting in Solid Tumors with Transferrin-Containing Gold Nanoparticles. *Proc. Natl. Acad. Sci. U.S.A.* **2010**, *107*, 1235–1240.
31. Kievit, F. M.; Veiseh, O.; Fang, C.; Bhattarai, N.; Lee, D.; Ellenbogen, R. G.; Zhang, M. Chlorotoxin Labeled Magnetic Nanovectors for Targeted Gene Delivery to Glioma. *ACS Nano* **2010**, *4*, 4587–4594.
32. Guy, C. T.; Cardiff, R. D.; Muller, W. J. Induction of Mammary Tumors by Expression of Polyomavirus Middle T Oncogene: A Transgenic Mouse Model for Metastatic Disease. *Mol. Cell. Biol.* **1992**, *12*, 954–961.
33. Thakur, M. L.; Devadhas, D.; Zhang, K. J.; Pestell, R. G.; Wang, C. G.; McCue, P.; Wickstrom, E. Imaging Spontaneous Mmtvneu Transgenic Murine Mammary Tumors: Targeting Metabolic Activity Versus Genetic Products. *J. Nucl. Med.* **2010**, *51*, 106–111.
34. Knutson, K. L.; Lu, H. L.; Stone, B.; Reiman, J. M.; Behrens, M. D.; Prosperi, C. M.; Gad, E. A.; Smorlesi, A.; Disis, M. L. Immunoediting of Cancers May Lead to Epithelial to Mesenchymal Transition. *J. Immunol.* **2006**, *177*, 1526–1533.
35. Leuschner, C.; Kumar, C. S.; Hansel, W.; Soboyejo, W.; Zhou, J.; Hormes, J. LHRH-Conjugated Magnetic Iron Oxide Nanoparticles for Detection of Breast Cancer Metastases. *Breast Cancer Res. Treat.* **2006**, *99*, 163–176.
36. Branca, R. T.; Cleveland, Z. I.; Fubara, B.; Kumar, C. S.; Maronpot, R. R.; Leuschner, C.; Warren, W. S.; Driehuys, B. Molecular MRI for Sensitive and Specific Detection of Lung Metastases. *Proc. Natl. Acad. Sci. U.S.A.* **2010**, *107*, 3693–3697.
37. Liu, J. C.; Deng, T.; Lehal, R. S.; Kim, J.; Zacksenhaus, E. Identification of Tumorsphere- and Tumor-Initiating Cells in HER2/Neu-Induced Mammary Tumors. *Cancer Res.* **2007**, *67*, 8671–8681.
38. Asiedu, M. K.; Ingle, J. N.; Behrens, M. D.; Radisky, D. C.; Knutson, K. L. Tgfbeta/Tnf(Alpha)-Mediated Epithelial-Mesenchymal Transition Generates Breast Cancer Stem Cells with a Claudin-Low Phenotype. *Cancer Res.* **2011**, *71*, 4707–4719.
39. Helmlinger, G.; Yuan, F.; Dellian, M.; Jain, R. K. Interstitial pH and pO2 Gradients in Solid Tumors *in Vivo*: High-Resolution Measurements Reveal a Lack of Correlation. *Nat. Med.* **1997**, *3*, 177–182.
40. Veiseh, O.; Gunn, J. W.; Kievit, F. M.; Sun, C.; Fang, C.; Lee, J. S.; Zhang, M. Inhibition of Tumor-Cell Invasion with Chlorotoxin-Bound Superparamagnetic Nanoparticles. *Small* **2009**, *5*, 256–264.